2.5D ELASTIC FINITE-DIFFERENCE MODELING

F.S. Neto, J. Costa, and A. Novais

email: *jesse@ufpa.br*

keywords: *elastic, finite-difference, modeling, anisotropy*

ABSTRACT

Finite difference modeling of elastic wavefields in 2.5D is described in the velocity-stress formulation for anisotropic media. The 2.5D modeling computes the 3D elastic wavefield in a medium which is translation invariant in one coordinate direction. The approach is appealing due reduced storage and computing time when compared to full 3D finite difference elastic modeling. The scheme handles inhomogeneities in mass density and elastic moduli, includes free-surface and perfect matched layers as absorbing boundaries. High order finite difference operator allows the use of a coarse mesh, reducing the storage even more without producing numerical dispersion and numerical anisotropy. Numerical experiments show the accuracy of the scheme, its computational efficiency and the importance of 2.5D modeling in complex elastic media.

INTRODUCTION

The 3D elastic modeling of seismic wavefields is very expensive and requires extensive computational resources, even for a modest-sized model. If the modeling of 3D wave propagation is carried out in media with only 2D variations in the material properties, the seismic line being positioned within the symmetry plane, this is generally referred to as the 2.5D situation. This situation is very interesting to numerical experiments as the medium symmetry can be used to reduce the complexity of the numerical task.

The modeling of seismic wave propagation in the 2.5D situation is helpful to approximately simulate seismic surveys along dip and strike directions in situations were full 3D modeling is unaffordable and where only 2D information about the medium is available. Some of these applications are conventional 2D seismic surveys, i.e., where the sources and receivers follow a single seismic line (Liner, 1991), and seismic borehole tomography (Williamson and Pratt, 1995).

Based on a Fourier transform of the acoustic wave equation in the out-of-plane direction, Song and Williamson (1995) presented an approach by repeated 2D finite-difference modeling in the frequency domain to find the exact solution of the 3D wave equation in the 2.5D situation for acoustic media with constant density, and applied their results to tomographic problems. They proved the quality of their results by a comparison to modeling with the Born approximation. Cao and Greenhalgh (1998) determined the stability and absorbing boundary conditions for this 2.5D FD approach, again for constant density, and compared the implementations in the time and frequency domains. In these papers, the inverse Fourier transform is carried out by a sum up to the Nyquist wavenumber. Recently, Novais and Santos (2005) revisited this approach for acoustic constant-density media and obtained stability conditions and sampling limits in the time domain as a function of the maximum wavenumber. Costa et al. (2005) extended these results to variable density, i.e., to any arbitrary acoustic media.

In this work, we transfer the time domain version of Novais and Santos (2005) to inhomogeneous elastic and anisotropic media with arbitrary symmetry class. The sources and receivers are not constrained to be within the same vertical plane. The velocity-stress formulation allows the computation of the complete elastic wavefield. In the general case, a complex valued system of equations needs to be solved. If sources and receivers are in the same vertical plane, the medium and the source distributions have mirror symmetry

across the vertical plane. Then, it is possible, with a change of variables, to reduce the system of equations to be solved to a real valued one. We present the stability conditions for the corresponding higher-order finite-difference schemes and derive the perfect matched layer (PML) absorbing boundary conditions. We validate the 2.5D algorithm against 3D finite-difference modeling. The 2.5D FD modeling can be implemented efficiently on parallel platforms. The formulation belongs to the class of embarrassingly parallel problems and the computation time reduces proportional to the number of processes.

METHOD

We solve the elastic field equations (Mittet, 2002; Minkoffy, 2002)

$$\rho(\mathbf{x})\frac{\partial v_i(\mathbf{x},t)}{\partial t} = \frac{\partial \sigma_{ij}(\mathbf{x},t)}{\partial x_j} + f_i(\mathbf{x},t) + \frac{\partial M^A_{ij}(\mathbf{x},t)}{\partial x_j}\,, \tag{1}$$

$$\frac{\partial \sigma_{ij}(\mathbf{x},t)}{\partial t} = C_{ijkl}(\mathbf{x})\frac{\partial v_k(\mathbf{x},t)}{\partial x_l} + \frac{\partial M^S_{ij}(\mathbf{x},t)}{\partial t}\,, \tag{2}$$

where ρ is the medium density, and v_i and f_i are the components of the vectorial velocity field and volume density force distribution, respectively. Moreover, C_{ijkl} denotes the components of the medium stiffness tensor, and σ_{ij} those of the stress tensor. Finally, M^S_{ij} and and M^A_{ij} are the components of the symmetric and anti-symmetric parts of the moment density tensor. These parts represent source distributions of volume-injection or double-couple type (M^S_{ij}) and of dipole type (M^A_{ij}).

In 2.5D modeling, one assumes the medium to be translation invariant along a coordinate direction, generally represented by x_2. In this case it is convenient to represent the elastic field and the sources distribution in the Fourier domain as

$$v_i(\mathbf{x},t) = \int_{-\infty}^{\infty} v_i(\mathbf{X},k_2,t)\exp\left(ik_2x_2\right)dx_2\,, \tag{3}$$

and

$$\sigma_{ij}(\mathbf{x},t) = \int_{-\infty}^{\infty} \sigma_{ij}(\mathbf{X},k_2,t)\exp\left(ik_2x_2\right)dx_2\,, \tag{4}$$

where k_2 is the wavenumber associated with x_2 and $\mathbf{X} \equiv (x_1, x_3)$. Also, $v_i(\mathbf{X},k_2,t)$ and $\sigma_{ij}(\mathbf{X},k_2,t)$ are the complex valued components of the respective fields in the k_2 wavenumber domain. Similarly, the source distributions can also be represented in the Fourier domain. Avoiding the introduction of new notational symbols, we denote from now on $v_i \equiv v_i(\mathbf{X},k_2,t)$, $\sigma_{ij} \equiv \sigma_{ij}(\mathbf{X},k_2,t)$, $f_i \equiv f_i(\mathbf{X},k_2,t)$, $M^A_{ij} \equiv M^A_{ij}(\mathbf{X},k_2,t)$, and $M^S_{ij} \equiv M^S_{ij}(\mathbf{X},k_2,t)$. The Fourier components of the elastic field and their source distribution obey, in an arbitrary anisotropic elastic medium, the complex valued system of equations

$$\rho(\mathbf{X})\frac{\partial v_i}{\partial t} = \frac{\partial \sigma_{iJ}}{\partial X_J} + i\,k_2\sigma_{i2} + f_i + \frac{\partial M^A_{iJ}}{\partial X_J} + i\,k_2M^A_{i2}\,, \tag{5}$$

$$\frac{\partial \sigma_{ij}}{\partial t} = C_{ijkL}(\mathbf{X})\frac{\partial v_k}{\partial X_L} + i\,k_2C_{ijk2}(\mathbf{X})v_k + \frac{\partial M^S_{ij}}{\partial t}\,, \tag{6}$$

where uppercase subscripts assume values 1 and 3 only. The summation convention also holds for these indices. This system of equations can be discretized in $\mathbf{X}$ and time and solved by finite differences.

We have implemented this algorithm for isotropic media. In this case, the stress field equations reduce to

$$\begin{aligned}
\frac{\partial \sigma_{11}}{\partial t} &= \lambda\left(\frac{\partial v_1}{\partial x_1} + ik_2v_2 + \frac{\partial v_3}{\partial x_3}\right) + 2\mu\frac{\partial v_1}{\partial x_1} + M^S_{11}\,,\\
\frac{\partial \sigma_{22}}{\partial t} &= \lambda\left(\frac{\partial v_1}{\partial x_1} + ik_2v_2 + \frac{\partial v_3}{\partial x_3}\right) + 2\mu ik_2v_2 + M^S_{22}\,,\\
\frac{\partial \sigma_{33}}{\partial t} &= \lambda\left(\frac{\partial v_1}{\partial x_1} + ik_2v_2 + \frac{\partial v_3}{\partial x_3}\right) + 2\mu\frac{\partial v_3}{\partial x_3} + M^S_{33}\,,
\end{aligned}$$

$$\begin{aligned}
\frac{\partial \sigma_{23}}{\partial t} &= \mu\left(\frac{\partial v_2}{\partial x_3} + ik_2 v_3\right) + M^S_{23}\,, \\
\frac{\partial \sigma_{13}}{\partial t} &= \mu\left(\frac{\partial v_1}{\partial x_3} + \frac{\partial v_3}{\partial x_1}\right) + M^S_{13}\,, \\
\frac{\partial \sigma_{12}}{\partial t} &= \mu\left(\frac{\partial v_2}{\partial x_1} + ik_2 v_1\right) + M^S_{12}\,,
\end{aligned} \tag{7}$$

where $\lambda = \lambda(\mathbf{X})$ and $\mu = \mu(\mathbf{X})$ are the Lamé parameters.

These equations are solved by finite differences in a staggered grid (Levander, 1988) for each value of k_2. We use a second-order approximation for the time derivatives and high-order approximations for the space derivatives. After solving the system above by finite differences, the elastic field components at the receivers position, $\mathbf{x}^R$, are computed as

$$\left[\begin{array}{c} v_i \\ \sigma_{ij} \end{array}\right](\mathbf{x}^R, t) = \int_{-\infty}^{+\infty} \left[\begin{array}{c} v_i \\ \sigma_{ij} \end{array}\right](x_1^R, k_2, x_3^R, t)\exp(ik_2 x_2^R)dk_2.$$

For volume injections sources, volume density forces, and dipole density moment tensors polarized in the x_1-x_3-plane, this system of equations can be reduced to a real valued system. This reduction is not possible for general anisotropic media and arbitrarily polarized source distributions, as presented above. As a consequence of the symmetry of the medium and the sources around the plane $x_2 = 0$, the field components v_2, σ_{12} and σ_{23} are odd functions of x_2, and their Fourier transform are purely imaginary. All the other field components are even functions of x_2 and have real Fourier transforms.

Defining the real quantities,

$$\begin{aligned}
u_2(x_1, k_2, x_3) &\equiv iv_2(x_1, k_2, x_3), \\
\tau_{12}(x_1, k_2, x_3) &\equiv i\sigma_{12}(x_1, k_2, x_3), \\
\tau_{23}(x_1, k_2, x_3) &\equiv i\sigma_{23}(x_1, k_2, x_3),
\end{aligned}$$

the final equations for 2.5D elastic modeling, in this particular case, are

$$\begin{aligned}
\frac{\partial v_1}{\partial t} &= \frac{1}{\rho}\left[\frac{\partial \sigma_{11}}{\partial x_1} + k_2\tau_{12} + \frac{\partial \sigma_{13}}{\partial x_3}\right] + \frac{1}{\rho}f_1 + \frac{\partial M_{1J}}{\partial x_J}, \\
\frac{\partial u_2}{\partial t} &= \frac{1}{\rho}\left[\frac{\partial \tau_{12}}{\partial x_1} - k_2\sigma_{22} + \frac{\partial \tau_{23}}{\partial x_3}\right], \\
\frac{\partial v_1}{\partial t} &= \frac{1}{\rho}\left[\frac{\partial \sigma_{13}}{\partial x_1} + k_2\tau_{23} + \frac{\partial \sigma_{33}}{\partial x_3}\right] + \frac{1}{\rho}f_3 + \frac{\partial M^A_{3J}}{\partial x_J}, \\
\frac{\partial \sigma_{11}}{\partial t} &= \lambda\left(\frac{\partial v_1}{\partial x_1} + k_2 u_2 + \frac{\partial v_3}{\partial x_3}\right) + 2\mu\frac{\partial v_1}{\partial x_1} + M^S_{11}, \\
\frac{\partial \sigma_{22}}{\partial t} &= \lambda\left(\frac{\partial v_1}{\partial x_1} + k_2 u_2 + \frac{\partial v_3}{\partial x_3}\right) + 2\mu k_2 u_2 + M^S_{22}, \\
\frac{\partial \sigma_{33}}{\partial t} &= \lambda\left(\frac{\partial v_1}{\partial x_1} + k_2 u_2 + \frac{\partial v_3}{\partial x_3}\right) + 2\mu\frac{\partial v_3}{\partial x_3} + M^S_{33}, \\
\frac{\partial \tau_{23}}{\partial t} &= \mu\left(\frac{\partial u_2}{\partial x_3} - k_2 v_3\right), \\
\frac{\partial \sigma_{13}}{\partial t} &= \mu\left(\frac{\partial v_1}{\partial x_3} + \frac{\partial v_3}{\partial x_1}\right) + M^S_{13}, \\
\frac{\partial \tau_{12}}{\partial t} &= \mu\left(\frac{\partial u_2}{\partial x_1} - k_2 v_1\right)\,.
\end{aligned} \tag{8}$$

The velocity field components v_1 and v_3, for receivers located in the plane $x_2 = 0$, reduce to

$$v_I(x_1^R, 0, x_3^R, t) = \int_{-\infty}^{+\infty} v_I(x_1^R, k_2, x_3^R, t)dk_2. \tag{9}$$

The extension of this simplification to anisotropic media where the plane $x_2 = 0$ is a plane of mirror symmetry is straightforward. In our implementation, the free-surface boundary condition is used at the top surface (Mittet, 2002) and PML absorbing boundaries (Chew and Liu, 1996) are imposed at the bottom and lateral boundaries. The PML equations are presented in the Appendix. The stability condition for the 3D finite difference scheme (Costa et al., 2005) is

$$\Delta t \leq \sqrt{\frac{2}{3d_0^{(2)}}}\frac{\Delta x}{c_P}\,, \tag{10}$$

where Δt is the time step, Δx is the grid space, and c_P is the P-wave velocity. Moreover,

$$d_0^{(2)} = \sum_{j=-N+1}^{N+1} d_j,$$

where d_j are the coefficients of the finite-difference operator for first derivatives, with N equal to the order of the finite difference approximation. If we require the 2.5D scheme to obey equation (9) (Novais and Santos, 2005), we can determine the maximum value for the wavenumber as (Silva Neto, 2004)

$$k_{2\max} \leq \frac{\sqrt{2d_0^{(2)}}}{\Delta x}. \tag{11}$$

The wavenumber sampling is $\Delta k_2 = 2\pi/\min(N_1, N_3)$, where N_1 and N_3 are the numbers of grid points in the x_1 and x_3 directions. When using FD schemes of order higher than 12, the spatial sampling to avoid numerical dispersion must satisfy

$$\Delta x \leq \frac{1}{3}\frac{C_{S\min}}{f_{\max}},$$

where $C_{S\min}$ is the minimum S-wave velocity and $f_{\max}$ is the upper limit of the wavelet's frequency band.

NUMERICAL EXPERIMENTS

The complex and real valued equation systems (7) and (8) for 2.5D elastic modeling were implemented on a serial platform and on a PC cluster. The parallel implementation is very efficient. Each of the equation systems (7) and (8) is solved for each wavenumber in a different process. There is no communication between processes until the FD has finished. As a consequence, the computation time for parallel implementation is the computation time of the serial implementation divided by the number of processes. In all the numerical experiments, we have modeled point sources using a Gaussian distribution around the source point

$$\begin{bmatrix} f_i \\ M_{ij} \end{bmatrix} = \begin{bmatrix} f_0(t)\, e_i \\ M_0(t)\, d_{ij} \end{bmatrix} \frac{1}{(2\pi h^2)^{3/2}} \exp\left(\frac{-\|\mathbf{x}-\mathbf{x}_s\|^2}{2h^2}\right),$$

where $f_0(t)$ is the pulse, e_i is the unit polarization vector for the volume-force density, $M_0(t)$ is the pulse and d_{ij} depends on the source type. For explosive sources, $d_{ij} = \delta_{ij}$, and for double couple sources, $d_{ij} = n_i\nu_j + n_j\nu_i$, where the unit vector n_i is normal to the fault plane and the unit vector ν_i is perpendicular to n_i (Aki and Richards, 1980; Minkoffy, 2002).

Homogeneous halfspace

We have computed the elastic wavefield in a homogeneous halfspace with a free surface as originating from a volume injection point source. The model has density 2000 kg/m^3, P-wave velocity 2500 m/s and S-wave velocity 1200 m/s. The source is 10 m below the surface and the wavelet is a Ricker with 10 Hz of peak frequency. Figures 1 and 2 compare the results of 2.5D and 2D elastic modeling after 0.5 s of propagation. These figures show the differences in relative amplitudes and wave shape among events. Figure 3 shows the snapshot of the velocity field after 0.6 s computed using the 2.5D algorithm. We observe the good performance of the PML absorbing boundary conditions.

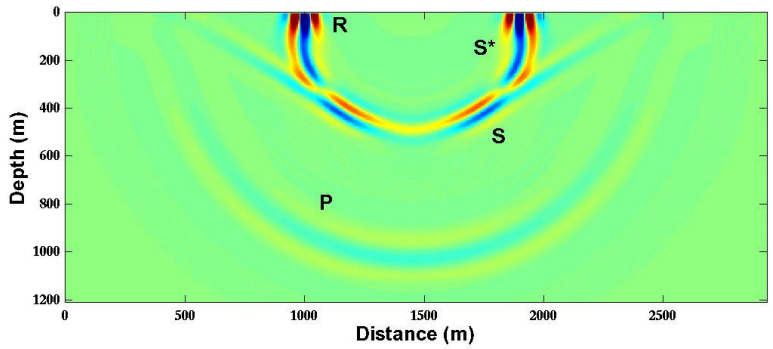

Figure 1: Vertical component of velocity wavefield after 0.5 s of propagation in a homogeneous halfspace with a free surface, computed by 2.5D elastic FD modeling. The Rayleigh wave (R), P wave, S wave and the S* wave are labeled.

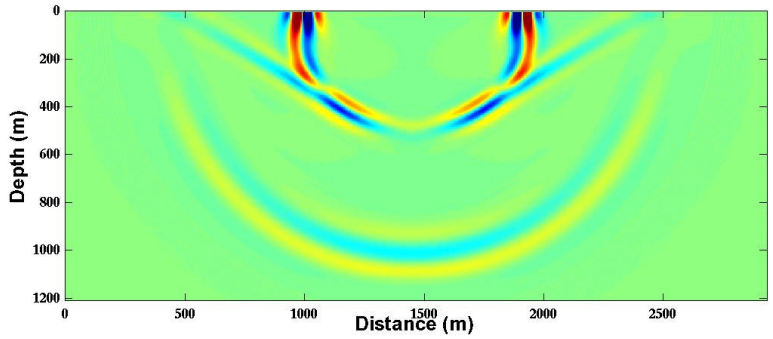

Figure 2: Vertical component of the velocity wavefield after 0.5 s of propagation computed using 2D elastic modeling. Observe the differences in the pulse width and shape and the relative amplitudes among the events as compared with the 2.5D result.

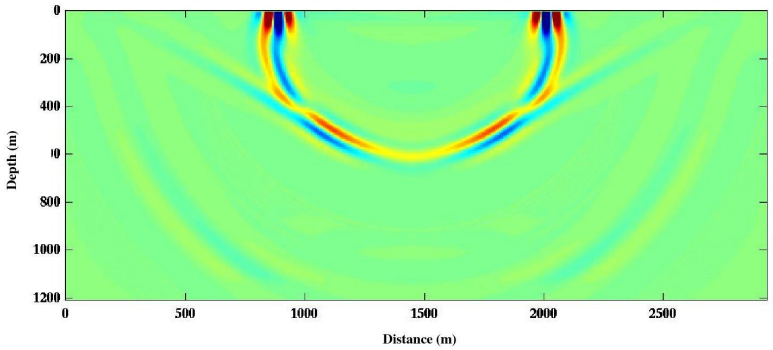

Figure 3: Vertical component of velocity wavefield after 0.6 s of propagation in a homogeneous halfspace with a free surface, computed by 2.5D elastic modeling. The PML absorbing boundary condition performs well attenuating the P wave at the bottom.

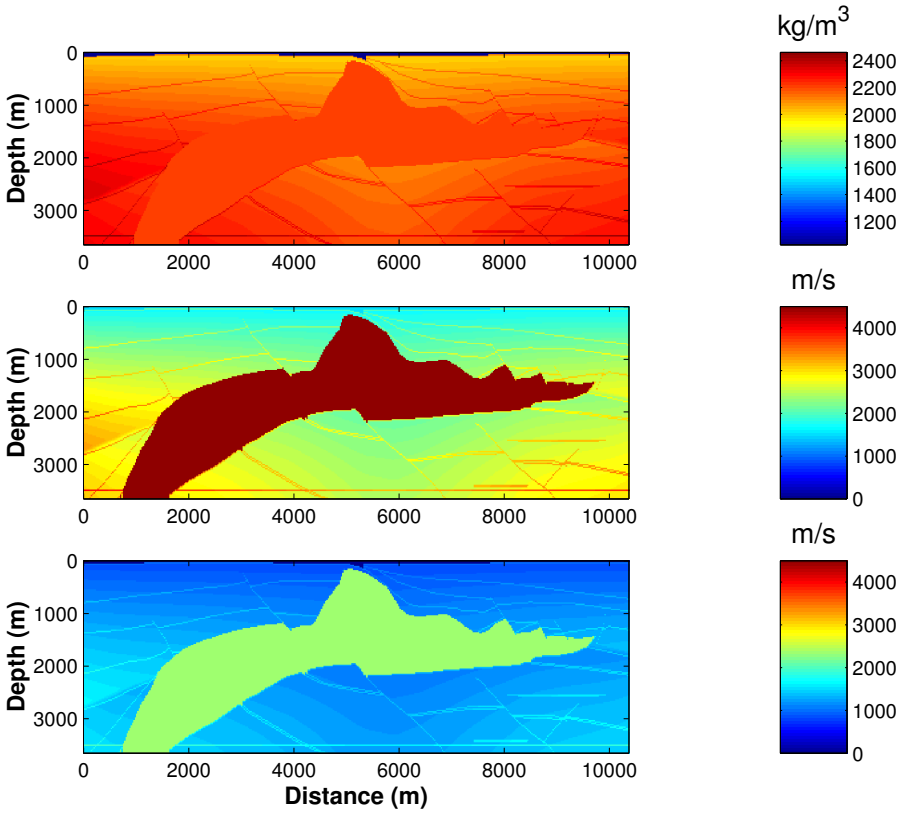

Figure 4: Density, P-wave, and S-wave velocity at a section of the SEG/EAEGE salt model.

SEG/EAGE salt model

We compare the results of 2D and 2.5D elastic finite difference modeling for the section of the SEG/EAGE model in Figure 4. The density and shear velocity were estimated using the prescription of House et al. (2000). Full 3D elastic modeling of a seismic survey in this model is still a challenge for today's computer hardware. The section we use for 2.5D modeling is sampled in a regular mesh of 10 m spacing with 365 by 1001 nodes. We simulate 1.5 seconds of propagation for an explosive source at 10 m depth, 300 receivers are located symmetrically around the source spaced by 20 m with 150 m minimum offset. The source pulse is a Blackman-Harris wavelet with peak frequency of 10 Hz. PML boundaries on the lateral and at the bottom have 21 grid nodes. Figure 5 presents the results of 2D and 2.5D modeling. The anomalous amplitudes, frequency content and phase of the 2D modeling are evident. In this case some events show a larger mismatch than others indicating the shortcomings of 2D modeling in complex inhomogeneous models.

Salt dome model

We also compare 2.5D and 3D elastic FD modeling in a simple salt dome model presented in Figure 6. The section we use is sampled in a regular mesh of 10 m spacing with 250 by 501 nodes. We have simulated 1.3 s of propagation for a explosive source at 10 m depth, 120 receivers are located symmetrically around the source, spaced by 20 m with 150 m minimum offset. For the 3D elastic simulation, 151 sections were replicated along the transversal direction and the line along source and receivers were positioned in the middle of the model. PML layers are applied on the bottom and on the lateral boundaries, each with a width of 21 grid points. Figure 7 contains the results of 2.5D and 3D elastic modeling. The two results present a very good agreement.

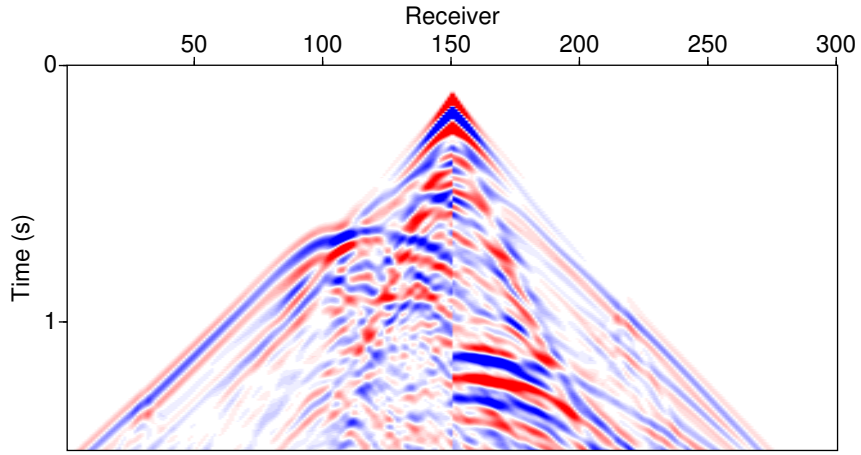

(a)

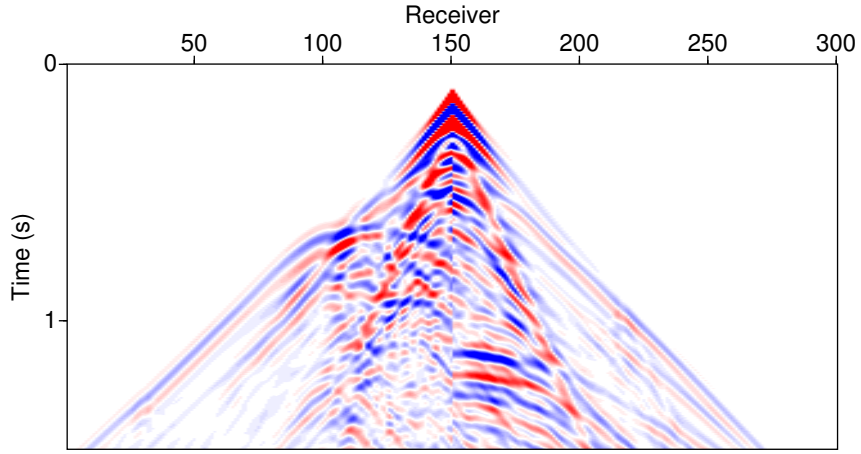

(b)

Figure 5: Vertical component of the velocity field after finite difference modeling using the section of SEG/EAGE salt model in Figure 4; (a) using a 2D FD, and (b) using the 2.5D FD. The 2D results present anomalous amplitudes and frequency content.

CONCLUSIONS

Full 3D elastic FD modeling is challenging even for today's PC clusters. We presented the formulation of 2.5D numerical modeling in arbitrary elastic media. Our approach to 2.5D modeling computes the complete elastic wavefield and handles arbitrary anisotropy. Stability conditions and PML absorbing boundary conditions for the FD algorithm were derived. The algorithm was successfully validated in complex inhomogeneous models against a full 3D elastic FD modeling. We believe this algorithm for 2.5D modeling is an accurate, low storage, alternative for seismic modeling whenever translation invariance along a strike direction can be assumed from geology. In such cases the 2.5D approach can compute the 3D wavefield for models specified in dense grids in a single PC. The 2.5D elastic modeling is very efficient in parallel platforms as compared to domain decomposition approaches to 3D FD elastic modeling.

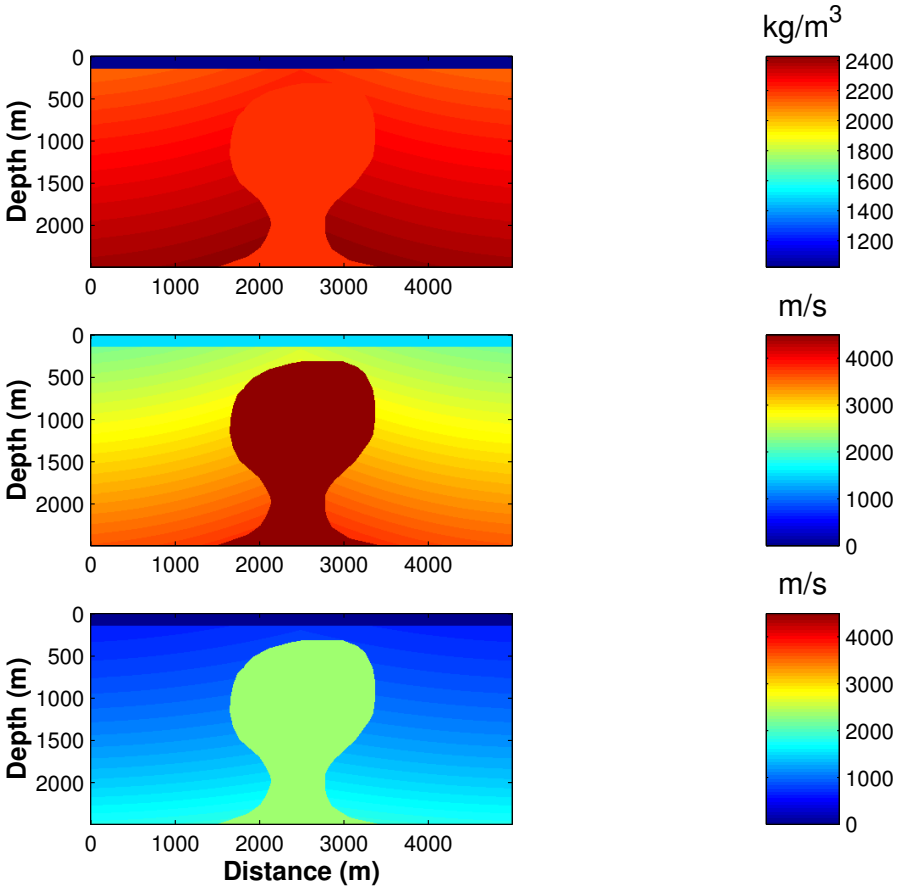

Figure 6: Density, P-wave, and S-wave velocity for a simple salt model.

ACKNOWLEDGMENTS

This work is supported by FINEP/CNPq and PETROBRAS through the project "Rede Cooperativa de Pesquisa em Risco Exploratório," as well as by the sponsors of the Wave Inversion Technology (WIT) Consortium.

REFERENCES

Aki, K. and Richards, P. (1980). *Quantitative Seismology – Vol. 1: Theory and Methods*. W.H. Freeman, New York.

Cao, S. and Greenhalgh, S. (1998). 2.5-D modeling of seismic wave propagation: Boundary condition, stability criterion, and efficiency. *Geophysics*, 63(6):2082–2090.

Chew, W. and Liu, H. Q. (1996). Perfectly matched layers for elastodynamics: a new absorbing boundary condition. *J. Computational. Acoust.*, 4(4):341–359.

Costa, J., Novais, A., Silva Neto, F. A., and Tygel, M. (2005). 2.5D acoustic finite-difference modeling in variable density media. *Journal of Seismic Exploration*, 13:323–335.

House, L., Larsen, S., and Bednar, J. B. (2000). 3D elastic numerical modeling of a complex salt structure. In *Expanded Abstracts*, volume 19, pages 965–968. SEG.

Levander, A. R. (1988). Fourth-order finite-difference P-SV seismograms. *Geophysics*, 53(11):1425–1436.

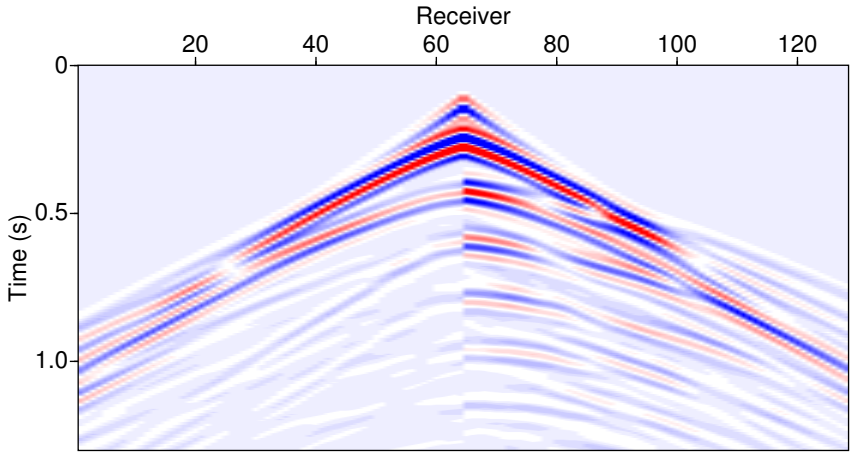

(a)

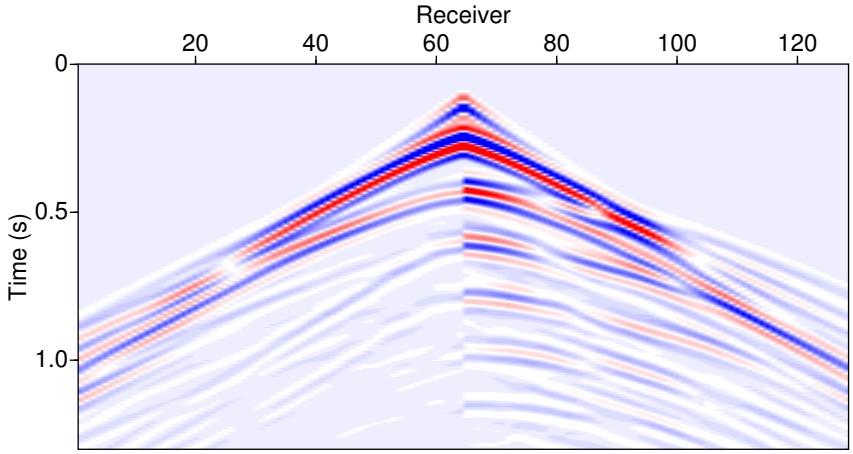

(b)

Figure 7: Pressure field after FD modeling for the simple salt model in Figure 6; (a) using a 2.5D FD, and (b) using the 3D FD.

Minkoffy, S. E. (2002). Spatial parallelism of a 3D finite difference velocity-stress elastic wave propagation code. *SIAM J. Sci. Comput.*, 24(1):1–19.

Mittet, R. (2002). Free-surface boundary conditions for staggered-grid modeling schemes. *Geophysics*, 67(5):1616–1623.

Novais, A. and Santos, L. (2005). 2.5D finite-difference solution of the acoustic wave equation. *Geophysical Prospecting*, 53:1–9.

Silva Neto, F. A. (2004). *Modelagem acústica por diferenças finitas e elementos finitos em 2-D e 2,5-D*. PhD thesis, CPGF-UFPA, Brazil. in Portuguese.

Song, Z. and Williamson, P. R. (1995). Frequency-domain acoustic-wave modeling and inversion of cross-hole data: Part I—2.5-D modeling method. *Geophysics*, 60(3):784–795.

Williamson, P. R. and Pratt, R. G. (1995). A critical review of acoustic wave modeling procedures in 2.5 dimensions. *Geophysics*, 60(2):591–595.

APPENDIX A

PERFECT MATCHED LAYERS (PML)

We use PML layers around the lateral and bottom boundaries of the model to reduce edge effects. Following Chew and Liu (1996), we assume that each velocity wavefield at the PML layers decomposed as

$$v_i = v_i^1 + v_i^2 + v_i^3 ,$$

and accordingly the stress field

$$\sigma_{ij} = \sigma_{ij}^1 + \sigma_{ij}^2 + \sigma_{ij}^3 ,$$

where the superscripts indicate a coordinate direction. Using the complex stretch method of Chew and Liu (1996), we derive the following equations for the field components in a general anisotropic medium:

$$\begin{aligned}
\frac{\partial v_1^1}{\partial t} + \gamma_1(x_1) v_1^1 &= \frac{1}{\rho}\left(\frac{\partial \sigma_{11}}{\partial x_1}\right), \\
\frac{\partial v_1^2}{\partial t} &= \frac{1}{\rho} i k_2 \sigma_{12}, \\
\frac{\partial v_1^3}{\partial t} + \gamma_3(x_3) v_1^3 &= \frac{1}{\rho}\left(\frac{\partial \sigma_{13}}{\partial x_3}\right), \\
\frac{\partial v_2^1}{\partial t} + \gamma_1(x_1) u_2^1 &= \frac{1}{\rho}\left(\frac{\partial \sigma_{12}}{\partial x_1}\right), \\
\frac{\partial v_2^2}{\partial t} &= \frac{1}{\rho} i k_2 \sigma_{22}, \\
\frac{\partial v_2^3}{\partial t} + \gamma_3(x_3) v_2^3 &= \frac{1}{\rho}\left(\frac{\partial \sigma_{23}}{\partial x_3}\right), \\
\frac{\partial v_3^1}{\partial t} + \gamma_1(x_1) v_3^1 &= \frac{1}{\rho}\left(\frac{\partial \sigma_{13}}{\partial x_1}\right), \\
\frac{\partial v_3^2}{\partial t} &= \frac{1}{\rho} i k_2 \sigma_{23}, \\
\frac{\partial v_3^3}{\partial t} + \gamma_3(x_3) v_3^3 &= \frac{1}{\rho}\left(\frac{\partial \sigma_{33}}{\partial x_3}\right), \\
\frac{\partial \sigma_{11}^1}{\partial t} + \gamma_1(x_1) \sigma_{11}^1 &= C_{11}\frac{\partial v_1}{\partial x_1} + C_{16}\frac{\partial v_2}{\partial x_1} + C_{15}\frac{\partial v_3}{\partial x_1}, \\
\frac{\partial \sigma_{11}^2}{\partial t} &= i k_2 \left(C_{16} v_1 + C_{12} v_2 + C_{14} v_3\right), \\
\frac{\partial \sigma_{11}^3}{\partial t} + \gamma_3(x_3) \sigma_{11}^3 &= C_{15}\frac{\partial v_1}{\partial x_3} + C_{14}\frac{\partial v_2}{\partial x_3} + C_{13}\frac{\partial v_3}{\partial x_3}, \\
\frac{\partial \sigma_{22}^1}{\partial t} + \gamma_1(x_1) \sigma_{22}^1 &= C_{12}\frac{\partial v_1}{\partial x_1} + C_{16}\frac{\partial v_2}{\partial x_1} + C_{25}\frac{\partial v_3}{\partial x_1}, \\
\frac{\partial \sigma_{22}^2}{\partial t} &= i k_2 \left(C_{26} v_1 + C_{22} v_2 + C_{24} v_3\right) \\
\frac{\partial \sigma_{22}^3}{\partial t} + \gamma_3(x_3) \sigma_{22}^3 &= C_{25}\frac{\partial v_1}{\partial x_3} + C_{24}\frac{\partial v_2}{\partial x_3} + C_{23}\frac{\partial v_3}{\partial x_3}, \\
\frac{\partial \sigma_{33}^1}{\partial t} + \gamma_1(x_1) \sigma_{33}^1 &= C_{13}\frac{\partial v_1}{\partial x_1} + C_{36}\frac{\partial v_2}{\partial x_1} + C_{35}\frac{\partial v_3}{\partial x_1}, \\
\frac{\partial \sigma_{33}^2}{\partial t} &= i k_2 \left(C_{36} v_1 + C_{23} v_2 + C_{34} v_3\right), \\
\frac{\partial \sigma_{33}^3}{\partial t} + \gamma_3(x_3) &= C_{35}\frac{\partial v_1}{\partial x_3} + C_{34}\frac{\partial v_2}{\partial x_3} + C_{33}\frac{\partial v_3}{\partial x_3},
\end{aligned}$$

$$
\begin{aligned}
\frac{\partial \sigma_{23}^1}{\partial t} + \gamma_1(x_1)\sigma_{33}^1 &= C_{14}\frac{\partial v_1}{\partial x_1} + C_{45}\frac{\partial v_2}{\partial x_1} + C_{45}\frac{\partial v_3}{\partial x_1}, \\
\frac{\partial \sigma_{23}^2}{\partial t} &= ik_2\left(C_{46}v_1 + C_{24}v_2 + C_{44}v_3\right), \\
\frac{\partial \tau_{23}^3}{\partial t} + \gamma_3(x_3)\tau_{23}^3 &= C_{45}\frac{\partial v_1}{\partial x_3} + C_{44}\frac{\partial v_2}{\partial x_3} + C_{34}\frac{\partial v_3}{\partial x_3}, \\
\frac{\partial \sigma_{13}^1}{\partial t} + \gamma_1(x_1)\sigma_{13}^1 &= C_{15}\frac{\partial v_1}{\partial x_1} + C_{56}\frac{\partial v_2}{\partial x_1} + C_{55}\frac{\partial v_3}{\partial x_1}, \\
\frac{\partial \sigma_{13}^3}{\partial t} + \gamma_3(x_3)\sigma_{13}^3 &= C_{55}\frac{\partial v_1}{\partial x_3} + C_{45}\frac{\partial v_2}{\partial x_3} + C_{35}\frac{\partial v_3}{\partial x_3}, \\
\frac{\partial \sigma_{13}^2}{\partial t} &= ik_2\left(C_{56}v_1 + C_{25}v_2 + C_{45}v_3\right), \\
\frac{\partial \sigma_{12}^1}{\partial t} + \gamma_1(x_1)\sigma_{12}^1 &= C_{16}\frac{\partial v_1}{\partial x_1} + C_{66}\frac{\partial v_2}{\partial x_1} + C_{56}\frac{\partial v_3}{\partial x_1}, \\
\frac{\partial \tau_{12}^2}{\partial t} &= ik_2\left(C_{66}v_1 + C_{26}v_2 + C_{46}v_3\right), \\
\frac{\partial \sigma_{12}^3}{\partial t} + \gamma_3(x_3)\sigma_{12}^3 &= C_{56}\frac{\partial v_1}{\partial x_3} + C_{46}\frac{\partial v_2}{\partial x_3} + C_{36}\frac{\partial v_3}{\partial x_3},
\end{aligned}
$$

where we are using the reduced notation for the stiffness tensor. The field attenuation at the absorbing boundaries are controlled by γ_1 and γ_3. For example, at the bottom γ_1 is zero and

$$
\gamma_3(x_3) = \begin{cases} \frac{(x_3 - x_3^0)^2}{L^2}, & \text{if } x_3 > x_3^0 \\ 0, & \text{otherwise.} \end{cases}
$$

Here, x_3^0 is the coordinate where the PML begins and L is its width. Likewise, for the lateral boundaries only γ_1 is not zero.